



High Frequency Communications Response to Solar Activity in September 2017 as Observed by Amateur Radio Networks

Nathaniel A. Frissell¹, Joshua S. Vega¹, Evan Markowitz¹,

Andrew J. Gerrard¹, William D. Engelke², Philip J. Erickson³,

Ethan S. Miller⁴, R. Carl Luetzelschwab⁵, and Jacob Bortnik⁶

Nathaniel A. Frissell, nathaniel.a.frissell@njit.edu

¹Center for Solar-Terrestrial Research,

New Jersey Institute of Technology,

Newark, NJ, USA

²University of Alabama, Tuscaloosa, AL,

USA

³Haystack Observatory, Massachusetts

Institute of Technology, Westford, MA, USA

⁴Johns Hopkins University Applied

Physics Laboratory, Laurel, MD, USA

⁵Independent Consultant, Fort Wayne,

IN, USA

This article has been accepted for publication and undergone full peer review but has not been through the copyediting, typesetting, pagination and proofreading process, which may lead to differences between this version and the Version of Record. Please cite this article as doi: 10.1029/2018SW002008

Abstract. Numerous solar flares and coronal mass ejection (CME) induced interplanetary shocks associated with solar active region AR12673 caused disturbances to terrestrial high frequency (HF, 3–30 MHz) radio communications from 4–14 September 2017. Simultaneously, Hurricanes Irma and Jose caused significant damage to the Caribbean Islands and parts of Florida. The coincidental timing of both the space weather activity and hurricanes was unfortunate, as HF radio was needed for emergency communications. This paper presents the response of HF amateur radio propagation as observed by the Reverse Beacon Network (RBN) and the Weak Signal Propagation Reporting Network (WSPRNet) to the space weather events of that period.

Distributed data coverage from these dense sources provided a unique mix of global and regional coverage of ionospheric response and recovery that revealed several features of storm-time HF propagation dynamics. X-class flares on 6, 7, and 10 September caused acute radio blackouts during the day in the Caribbean with recovery times of tens of minutes to hours, based on the decay time of the flare. A severe geomagnetic storm with $Kp_{max} = 8+$ and $SYM-H_{min} = -146$ nT occurring 7–10 September wiped out ionospheric communications first on 14 MHz and then on 7 MHz starting at ~ 1200

⁶Department of Atmospheric and Ocean Sciences, University of California, Los Angeles, CA, USA

UT 8 September. This storm, combined with affects from additional flare and geomagnetic activity, contributed to a significant suppression of effective HF propagation bands both globally and in the Caribbean for a period of 12 to 15 days.

Keypoints:

- Solar flares and geomagnetic storms disrupted high frequency (HF, 3–30 MHz) emergency radio communications in September 2017
- HF propagation recovered from solar flare radio blackouts in tens of minutes to hours
- HF propagation recovered from geomagnetic storms over a period of days

1. Introduction

High frequency (HF, 3–30 MHz) radio is a valuable method of electronic communications that does not require man-made infrastructure to relay messages over the horizon. Even in the modern age of space-borne relays and widely distributed Internet availability, HF radio remains a key technology for long distance communications. It is actively used by aircraft, by ships at sea, in military operations, for disaster relief efforts, and by amateur radio operators. HF radio is particularly attractive in a backup or emergency communications role because of its ad-hoc and agile nature, relatively low cost, and ability to communicate across large distances. In September 2017, HF amateur radio was called upon to provide emergency communications to the Caribbean Region in response to the devastation caused by Hurricanes Irma and Jose [ARRL, 2018].

Over-the-horizon HF communication between ground stations is made possible by radio wave refraction back to Earth by the ionosphere [Davies, 1990]. The ionospheric dependence of HF links means that dynamic space weather impacts on near-Earth plasma have a profound effect on HF propagation. As such, the United States National Oceanic and Atmospheric Administration (NOAA) issues alerts regarding specific adverse space weather conditions on a scale of 1 (minor), 2 (moderate), 3 (strong), 4 (severe), and 5 (extreme). This includes alerts for radio blackouts (R), geomagnetic storms (G), and solar radiation storms (S) [Poppe, 2000]. Unfortunately, the timing of Hurricanes Irma and Jose coincided with numerous solar flares and CME-induced interplanetary shocks originating from solar active region AR12673 that resulted in R3, G4, and S3 alerts and

ultimately impacted Earth and disrupted emergency HF communications [Redmon *et al.*, 2018].

Radio blackouts are the complete fading out of dayside HF radio transmissions for a period ranging from a few minutes to an hour or more [Dellinger, 1937]. Radio blackouts, also known as short-wave fadeouts (SWF), result from a sudden, solar flare-induced increase of extreme ultraviolet (EUV) and X-ray radiation that ionizes the D region and causes collisional absorption [Benson, 1964; McNamara, 1979]. Because EUV and X-ray energy propagate at the speed of light, it takes only approximately 8 minutes to reach the Earth and it is not possible to provide advanced warning of a geoeffective HF radio blackout. A recent study by Chakraborty *et al.* [2018] used SuperDARN HF radars to determine that the amount of HF radar echo suppression is a function of solar zenith angle, radio wave frequency, and flare intensity. Frissell *et al.* [2014] showed a near-total elimination of dayside amateur radio HF communications in response to an X2.9 class solar flare using observations from the amateur-operated Reverse Beacon Network.

Geomagnetic storms are changes in the Earth's magnetic field caused by solar wind particles with increased speed or density impacting the Earth's magnetosphere [Gonzalez *et al.*, 1994]. This fast and/or dense solar wind originates from either a coronal mass ejection (CME) or coronal hole. Enhanced electric fields, currents, and particle precipitation during geomagnetic storms are large-scale energy inputs to the upper atmosphere that lead to systematic changes in ionospheric densities known as ionospheric storms [Buonsanto, 1999; Prölss, 2008]. Ionospheric storms may be tracked by monitoring changes in the peak F2 electron density (NmF2) or the total electron content (TEC). In the midlatitude F region, ionospheric storms often have a positive phase (increases in $\text{NmF2}/\text{TEC}$) lasting

less than 24 hours, followed by a negative phase (decreases in NmF2/TEC) that may last multiple days [Matsushita, 1959; Mendillo, 2006]. These density changes are caused by changes in neutral atmospheric composition that retard or enhance ion production and loss rates and are driven by storm-time electrodynamic effects and neutral winds [Fuller-Rowell *et al.*, 1996; Rishbeth, 1998]. Ionospheric storm effects are dependent on season, UT time, and local time [Thomas *et al.*, 2016].

In this paper we present a study investigating the impacts of the September 2017 space weather events on HF communications using amateur radio data. Section 2 presents the data sources and methodology. Section 3 presents results and discussion of the impacts of solar flares on HF communications (Section 3.1), the impacts of geomagnetic disturbances on HF communications (Section 3.2), and the impacts on HF communications in the Caribbean Region (Section 3.3). Section 4 summarizes the findings.

2. Data and Methodology

2.1. Amateur Radio Data Sources

To monitor high frequency (HF) radio communications we use data from two separate automated amateur radio monitoring networks, the Reverse Beacon Network (RBN, reversebeacon.net) and the Weak Signal Propagation Reporting Network (WSPRNet, wsprnet.org). These networks operate continuously and are built, operated, and maintained on a volunteer basis by members of the amateur radio community. Recent technological advances, such as the development of software defined radios (SDRs) that rely primarily on digital signal processing techniques implemented in software have helped to enable these observation networks. Observations are archived and available for download at the respective website of each network. The RBN uses dedicated SDR receivers to simultane-

ously monitor and decode Morse code (a.k.a. continuous wave or CW) and radioteletype (RTTY) transmissions on amateur radio frequencies. WSPRNet utilizes an advanced digital communications scheme specifically created for monitoring ionospheric propagation [Taylor and Walker, 2010]. Typically, WSPRNet nodes have both transmit and receive capabilities. Both systems report the time, frequency, signal-to-noise ratio (SNR), and callsigns of the transmitting (TX) and receiving (RX) stations in a record known as a “spot”. WSPRNet will also provide the user-reported geographic location. When a user-reported location is not available, a lookup to a public database such as <http://qrz.com> or <http://hamcall.net> is made. If location is not provided and a database lookup is not available, the spot is discarded. All licensees in the United States are required to be in the database, and many international operators choose to be included. Location errors will occur if an operator chooses to transmit from different location from that specified in the database. The data in this paper consists of roughly 80% WSPRNet data, which includes a user-supplied location tag with each transmission.

WSPRNet and RBN databases date back to 2008/2009 and can be used as a source of citizen science crowd-sourced data for studying the effects of space weather and other phenomena on the structure and dynamics of the ionosphere [e.g. Frissell *et al.*, 2014, 2018]. In this paper, we use observations of the 1.8, 3.5, 7, 14, 21, and 28 MHz amateur radio bands. Table 1 shows the amateur radio frequency limits and approximate wavelength in meters for each of these bands. Amateur radio operators are only allowed to transmit on frequencies specifically authorized by their particular national government; these bands were chosen because they are internationally recognized amateur radio frequencies that sample many different regions of the medium and high frequency radio spectra. To show

geographic coverage and illustrate an example use case, Figure 1 shows ionospheric HF propagation paths extracted from RBN and WSPRNet data around the 6 September 2017 X9.3 class solar flare. Both panels show maps of point-to-point communications reports received by the reporting networks, color-coded by frequency. Figure 1a shows the 12,824 spots observed during the 15 minutes prior to the solar flare, while Figure 1b shows the less than 2,300 spots observed during the 15 minutes following the solar flare. Propagation path lines are drawn by determining the great circle path between the transmitter and receiver based on known geographic location associated with each of the relevant amateur call signs.

2.2. Geospace Environment Data Sources

In order to better understand the causes of disturbances in the crowd-sourced amateur radio observations, several scientific data sets provide measurements of space weather and geomagnetic conditions, including K_p , SYM-H, and the GOES XRS 0.1–0.8 nm soft X-ray flux datasets. K_p was obtained from the NASA Goddard Space Flight Center OMNIWeb [King and Papitashvili, 2006], SYM-H was obtained from the Kyoto World Data Center for Geomagnetism, and GOES XRS measurements were retrieved from the NOAA National Center for Environmental Information (NCEI). Each dataset provides a different and complementary view of space weather drivers and their effects in the ionosphere and magnetosphere.

The K_p index is a quasi-logarithmic scale from 0 to 9 that quantifies the level of geomagnetic disturbance [Menvielle and Berthelier, 1991]. This index is calculated using observations from 13 midlatitude ($\pm 44^\circ$ – 60° MLAT) ground magnetometers located in North America, Europe, and Australia. Hence, K_p is most indicative of geomagnetic con-

ditions in these regions. At each station, fluctuations in the strength of the horizontal component of the magnetic field are observed over a 3 hour interval. The resulting value is subsequently associated with an individual K value based on the geomagnetic latitude of the measurement station, such that a station near the equator requires less geomagnetic fluctuation than a station near the poles in order to record the same K value. Finally, the weighted mean of measurements from all K_p observatories allows calculation of a global K_p value.

The SYM-H index is a measure of disturbances from background in the low-latitude horizontal component of the magnetic field, and is considered a high-time resolution (1 min) version of the hourly Disturbance Storm Time Dst index [Sckopke, 1966; Iyemori, 1990; Wanliss and Showalter, 2006]. Observations from 6 out of 11 possible ground magnetometer stations evenly distributed in longitude and in the range of $\pm 10^\circ$ – 50° magnetic latitude contribute to the SYM-H index. SYM-H monitors the intensity of the magnetospheric ring current. A negative SYM-H value indicates an intensification of the ring current and is associated with geomagnetic storm activity.

In addition to the two previously described indices, data from the Geostationary Operational Environmental Satellite (GOES) system is also used. This consists of observations from the GOES-13 (GOES-EAST, $\theta = -75^\circ$ E) and GOES-15 (GOES-WEST, $\theta = -135^\circ$ E) platforms. Each satellite carries an X-Ray Sensor (XRS) providing 0.1–0.8 nm X-ray irradiance observations [Chamberlin et al., 2009]. A solar flare can cause sudden and unexpected fluctuations in solar X ray irradiance.

2.2.1. Total Electron Content

To compare amateur radio propagation observations to an independent measure of ionospheric content, we obtained Global Positioning System Total Electron Content (GPS TEC) data from the Massachusetts Institute of Technology CEDAR Madrigal database. This database includes daily observations from approximately 6,000 receivers worldwide and 2,000 in North America [Coster *et al.*, 2017]. GPS TEC provides a measure of electrons in a height-integrated column between a ground receiver and a GPS satellite at \sim 20,200 km altitude by measuring the dispersion between two frequencies, typically L1 (1575.42 MHz) and L2 (1227.60 MHz) [Coster and Komjathy, 2008]. Slant TEC is converted to vertical TEC and TEC biases are removed according to the algorithms described by Rideout and Coster [2006]. TEC is measured in TEC units (TECU), where $1 \text{ TECU} = 10^{16} \text{ electrons m}^{-2}$. TEC is well correlated to the F2 region peak plasma frequency (f_oF_2) [Davies and Liu, 1991; Krankowski *et al.*, 2007], and hence a useful predictor of HF propagation conditions. Additionally, GPS TEC is highly sensitive to ionospheric storms and has played a key role in the study of storm morphology and climatology [e.g., Foster *et al.*, 2002; Thomas *et al.*, 2013, 2016].

3. Results and Discussion

3.1. Solar Flare Impacts of 6 September 2017

On 6 September 2017, two X-class solar flares caused a significant disruption in terrestrial HF communications. Figures 2a and 2b show selected space weather environmental parameters from 0600 to 1800 UT. Figure 2a indicates an extended geomagnetically quiet period with $-8 \leq \text{SYM-H} \leq 18 \text{ nT}$ (black line) and $K_p \leq 3$ (colored stems). Figure 2b shows GOES-13 (blue) and GOES-15 (orange) XRS 0.1–0.8 nm X-ray measurements.

The onsets of an X2.2 class flare at 0857 UT and a more intense X9.3 class flare at 1153 UT are indicated with dotted vertical lines.

3.1.1. Solar Flare Impacts on HF Radio Over Europe

Europe was located in the daytime sector during the two X-class flares on 6 September 2017, and thus HF communications in this region were strongly affected by these flares. This is seen in Figures 2c–2f, which show 2D contour histograms of RBN and WSPRNet spot data for the 28, 21, 14, and 7 MHz frequency bands. Radio observations in Figure 2 were restricted to spots over Europe, here defined as spots having TX-RX midpoints with geographic latitudes between $30^\circ \leq \phi < 65^\circ$ N and longitudes between $-15^\circ \leq \theta < 55^\circ$ E. A map showing the logarithm of spot count [$\log(\# \text{ spot})$] density on a 1° by 1° grid of all spots used within a particular band is located to the left of each histogram. The underlying grid of the histogram is 10 min by 250 km. The great circle path length (R_{gc}) was further limited to 3000 km to show the most active ranges, which retained 98% of available spots. The white dashed curves on the histograms show the solar zenith angle computed for $(51^\circ \text{ N}, 8^\circ \text{ E})$, the point indicated by the yellow star on the center of each map. This point was determined using the center-of-mass function of the locations of all spots in Figure 2. Dotted vertical lines indicate the onset times of the X2.2 and X9.3 class flares that occurred during this interval.

Prior to the first flare at 0857 UT, moderate to substantial activity was observed on each band, with GOES X-ray flux levels between 1×10^{-6} and $5 \times 10^{-6} \text{ W}\cdot\text{m}^{-2}$. The most active bands were 7 and 14 MHz, which supported communication ranges R_{gc} centered at approximately 500 and 750 km, respectively. The 21 and 28 MHz bands became active as the solar zenith angle decreased and the MUF correspondingly increased, starting at

~0700 UT. Communication ranges R_{gc} on these bands were centered at ~1500–1700 km.

At the onset of the 0857 UT X2.2 class flare, all four bands experienced an abrupt drop-off in the number of spots. Flare recovery began within 15 minutes of flare onset. Even though the X-ray flux never returned to pre-flare levels, the 14, 21, and 28 MHz bands built up to stronger activity levels than observed prior to the 0857 UT flare, consistent with diurnal ion density variations. A second communication range on 14 MHz, potentially due to onset of favorable 2-hop propagation geometry, became more evident at $R_{gc} \approx 1750$ km between 1100–1200 UT. The 7 MHz band never recovered to pre-flare levels. The pre- and post-flare differences can likely be attributed to ionospheric diurnal variations, including increased D region absorption on 7 MHz and higher E and F region electron densities leading to increased support of 14, 21, and 28 MHz refraction. After the first recovery, a second, larger X9.3 class flare followed at 1153 UT. Once again, all of the HF activity over Europe dropped abruptly followed by a radio blackout. Unlike the first flare, this more intense event was not followed by HF recovery onset until approximately 1300 UT, an hour after the flare. Subsequently, Europe entered the dusk sector and the solar zenith angle increased, with a general reduction in ionospheric content and a return to normal diurnal propagation effects. These included an increase in the number of available 7 MHz paths and a decrease in usability of the higher frequency bands.

3.1.2. Solar Flare Impacts on HF Radio Over the United States

While Europe was on the dayside and therefore experiencing the full brunt of the multiple 6 September 2017 solar flares, the Continental United States (CONUS) was in the dawn sector at the edge of the flare illumination region. This resulted in a “grazing” geometry and led to fewer adverse effects for HF communications over the CONUS. Figure 3 shows

conditions at HF midpoints over the CONUS presented in the same format as Figure 2.

The CONUS region has been selected such that latitudes are between $20^\circ \leq \phi < 55^\circ$ N and longitudes are between $-130^\circ \leq \theta < -160^\circ$ E. 87% of available spots were retained when limiting $R_{gc} \leq 3000$ km. The white, dashed solar zenith angle curves of Figures 3c–3f are now computed for (39° N, -93° E), as indicated by the yellow star in the center of each CONUS map. Dotted vertical lines indicate the onset times of the X2.2 and X9.3 class flares that occur during the plotted interval.

The WSPRNet and RBN spot histograms of Figure 3 show that 7 and 14 MHz were the most active bands during the time of flare activity, with normal diurnal variations clearly visible. In particular, before the sun rose at approximately 1100 UT, ionospheric propagation was almost non-existent on 21 and 28 MHz and minimal on 14 MHz due to the low nighttime MUF. However, the 7 MHz band was highly active with the majority of spots centered at $R_{gc} \approx 1750$ km range. Once the sun rose and the solar zenith angle dropped below 90°, the MUF rose with a corresponding increase in D region absorption. The 7 MHz range decreased to $R_{gc} \approx 250$ km by 1130 UT, while 14 MHz showed strong activity between $750 \lesssim R_{gc} \lesssim 1750$ km starting at 1300 UT. After 1300 UT, ionospheric propagation appeared in the 21 and 28 MHz bands. The 0857 UT X2.2 class flare was observed by GOES while the CONUS was still in the nighttime sector. Figure 3e and 3f show that no discernible flare effects were observed at this time in either of the active bands, 7 MHz and 14 MHz. However, the 1153 UT X9.3 class flare coincides with an abrupt reduction in spot density at all R_{gc} on both the 7 and 14 MHz. Figures 3e and 3f show that these bands begin recovery from the X9.3 1153 UT flare within 10 to 15 minutes and achieve an apparent full recovery within an hour. This is in sharp contrast

to the almost 2 hr recovery observed in Figure 2 for Europe, which experienced this flare while in the noon sector.

Figures 2 and 3 showed that the RBN and WSPRNet spots stop abruptly in response to solar flares in a manner consistent with an increase in collisional damping from a sudden enhancement in D region ionospheric densities resulting from the X-ray radiation from the flare [Davies, 1990]. This response is strongest on the dayside, and typically all HF bands shown were affected. Although radio blackouts from a solar flare may be severe, the D region ionospheric recombination time is on the order of a few minutes and therefore HF propagation recovery typically takes place on the order of minutes to at most a few hours, based on the decay time of the flare. These observations are consistent with recent SuperDARN HF radar studies by *Chakraborty et al.* [2018].

3.2. Geomagnetic Storm Impacts

In addition to the solar flares on 6 September 2017, AR12673 also produced a large, geoeffective coronal mass ejection (CME) induced interplanetary shock on the same day. This shock arrived at Earth on 7 September 2017 and caused significant geomagnetic disturbances through 9 September 2017 [*Redmon et al.*, 2018]. These effects and the global HF radio propagation response are presented in Figure 4, which depicts the interval of 6–12 September 2017. Figure 4a shows the SYM-H (black line) and K_p (colored stems) indices. Figure 4b presents GOES-13 (blue) and GOES-15 (orange) XRS 0.1–0.8 nm X-ray measurements. Key times are marked with dotted vertical lines. Conditions were geomagnetically quiet until 2100 UT on 7 September 2017 and remained highly disturbed until 0000 UT on 9 September 2017. During this time, K_p reached a maximum of 8+ and

SYM-H reached a minimum of -146 nT, characteristic of a moderate to strong intensity storm. C, M, and X class flares were also present throughout the 6 day interval.

Figures 4c–4h show 2D contour time series histograms of RBN and WSPRNet spot data for the 28, 21, 14, 7, 3.5, and 1.8 MHz amateur radio bands. The histograms have an underlying grid of 30 min by 500 km bins. The range shown extends to $R_{gc} = 10000$ km so that long-distance communications can be observed, and a log scale is employed to enhance visibility of the lower-density spots at far ranges. To the left of each time series histogram is a density map showing the TX-RX midpoints in 1° latitude by 1° longitude bins of all spots used the corresponding time series. The radio data is heavily weighted in favor of the United States and Europe due to the distribution of radio amateurs, and this provides a strong diurnal modulation in spot density. Additionally, radio blackouts caused by solar flares as described in Section 3.1 occur throughout the interval.

A quiet time baseline was constructed from 2016 and 2017 RBN and WSPRNet spot data. Days with $-25 \leq \text{SYM-H} \leq 25$ nT and $K_p < 3$ were selected, for a total 283 quiet days. A time series histogram using a 30 min by 500 km grid was computed for each quiet day. Next, the mean μ and standard deviation σ for each bin was computed. Finally, the z -score ($z = (x - \mu)/\sigma$) for each bin x in Figures 4c–4h was calculated to determine the departure in standard deviations from the 2-year quiet time mean. Figure 5 shows these z -scores in the same format as Figure 4. In the time series histograms of Figures 5c–5h, red colors indicate above-average activity, blue colors indicate below-average activity, and white is average behavior for quiet time.

Geomagnetic storm effects are seen in the radio observations starting at 2100 UT September 7. This is coincident with a jump in K_p from 3- to 8-. SYM-H = 12 nT

and is starting its decent to a minimum of -146 nT. At this time (marked as the first dotted vertical line on Figures 4 and 5), a brief increase in spot density across ranges can be seen on 28, 21, 14, and 7 MHz (Figures 4c–4f), along with a corresponding brief positive departure in z -score in Figures 5c–5f. Immediately following, 21, 14, and 7 MHz (Figures 4d–4f) experience an abrupt dropoff in spot density that lasts until geomagnetic activity subsides, between 0000 and 1400 UT 9 September. Correspondingly, the z -scores of Figures 5d–5f show an extended period of departures below mean between 2100 UT September 7 and 1400 UT September 9, compared with the observations outside of this time period. Figures 4g–4h and 5g–5h show that 3.5 and 1.8 MHz are relatively unaffected by the storm. Figures 4a and 5a show anomalously strong patches of activity during storm time on 28 MHz.

The observations of Figures 4 and 5 are consistent with ionospheric storms occurring in the summer/equinoctial months [Thomas *et al.*, 2016]. Summer storms typically begin with a short positive phase followed by a deeper, longer negative phase. This is because negative storm effects occur in a “composition disturbance zone” (CDZ) that starts in the high latitudes. In the CDZ, an expansion of the thermosphere caused by storm time energy inputs causes an upwelling of $[N_2]$ and $[O_2]$ from F1 to F2 region heights. This increases the recombination rate to cause the negative effect. In the summer hemisphere, a prevailing transequatorial summer-to-winter thermospheric wind helps to propagate the CDZ across the equator and cause negative effects to dominate. In the winter hemisphere, the background poleward thermospheric wind opposes the CDZ, which can lead to a downwelling of $[O]$ from the F2 to F1 region and hence a higher rate of ion production when in sunlight [Fuller-Rowell *et al.*, 1996; Rishbeth, 1998].

In our case, 28, 21, 14, and 7 MHz all show a brief excursion above mean activity at multiple ranges in Figures 5c–5f consistent with an enhancement in F region ionization. The extended period of below-mean activity on the 21, 14, and 7 MHz bands (Figures 5d–5f) beginning at 2100 UT 7 September is consistent with a negative storm period causing the MUF to drop and render previously available link paths unusable. The enhancements on 28 MHz in Figure 5 during storm time are surprising, it is possible that the WSPR mode, which has excellent weak signal performance, is taking advantage of an above-the-MUF propagation mode [e.g., *McNamara et al.*, 2008; *Gibson and Bradley*, 1991]. It is not surprising, however, that the lowest bands, 3.5 and 1.8 MHz, are relatively unchanged as they are likely below the MUF, even during storm time. However, Figures 4g and 4h indicate that these bands tended to perform better only at shorter ranges ($R_{gc} \lesssim 2000\text{km}$) even during the geomagnetically quiet periods.

3.3. Impacts on Caribbean HF Communications

The space weather events of September 2017 posed serious difficulties to HF emergency communications by hurricane relief efforts in the Caribbean. The most significant storm of this period was Hurricane Irma, which made landfall as a Category 5 hurricane on 6 September 2017 on Barbuda and continued through the Caribbean Islands reaching the Florida Keys as a Category 4 hurricane on 10 September 2017. Irma then continued through Southwest Florida where it weakened to a Tropical Storm on 11 September [*weather.com*, 2017]. In response, the Hurricane Watch Net (HWN, www.hwn.org), a group of licensed Amateur Radio Operators trained and organized to provide essential communications support to the National Hurricane Center during times of hurricane emergencies, activated on 14.325 and 7.268 MHz [*ARRL*, 2017].

The likely impact to HF radio systems by space weather events can be summarized using the U.S. National Oceanic and Atmospheric Administration (NOAA) Space Weather Scales [Poppe, 2000]. These scales classify geomagnetic storms as a function of K_p on a scale from G1-minor ($K_p = 5$) through G5-extreme ($K_p = 9$), and solar flare radio blackouts from R1-minor (M1 class flare) through R5-extreme (X20 class flare). Figure 6 shows space weather environmental indices and HF amateur radio activity on 14 and 7 MHz observed by WSPRNet and the RBN in the Caribbean region from 4–14 September 2017. Dotted vertical lines mark key times in the figure. Figure 6a shows both SYM-H (black line) and K_p (colored stems) indices. The G3-strong ($K_p = 7$) / G4-severe ($K_p = 8 - 9+$) geomagnetic storm, described on a global context in Section 3.2, was observed from 7–9 September 2017, beginning at 2100 UT September 7. G1-minor geomagnetic storms were observed from 4–5 September and 12–13 September. Figure 6b shows GOES-13 (blue) and GOES-15 (orange) 0.1–0.8 nm X-ray measurements. Numerous R3-strong ($X1 \leq$ flare class $< X10$) radio blackout periods were observed throughout the interval, including those associated with the X2.2 class flare at 0857 UT 6 September and the X9.3 class flare at 1153 UT 6 September, as described in Section 3.1. Additional large flares observed in this interval include an X1.5 class flare at 1436 UT 7 September 2017 and the X8.2 class flare at 1535 UT 10 September 2017.

Figures 6c and 6d show the 14 and 7 MHz amateur radio bands observed by WSPRNet and the RBN in the Caribbean region from 4–14 September 2017. To emphasize the space weather impacts on communications systems rather than on the ionosphere, the spots selected for Figure 6 have been defined by link endpoints (either transmit or receive) rather than link midpoints. All spots were required to have at least one endpoint in the

Caribbean, defined here as a region bounded by latitudes between $17^\circ \leq \phi < 30^\circ$ N and longitudes between $-86^\circ \leq \theta < -65^\circ$ E. The small maps in Figure 6 show the endpoints of all spots for their respective bands for the entire 4–14 September 2017 interval. The black dots in each map represent endpoints contained within the Caribbean region (black box). The corresponding endpoints outside of the Caribbean region are identified by dots color-coded with the great circle path length R_{gc} of each link. Each time series consists of a contour histogram of log spot density with an underlying grid of 10 min by 250 km bins. The white dashed lines on the histograms show the solar zenith angle computed for (24° N, -76° E), the point indicated by the yellow star in the center of the Caribbean box. The 28, 21, 3.5, and 1.8 MHz bands are not shown as they each have < 1000 spots for the entire interval.

The amateur radio observations of Figure 6 clearly show the expected diurnal variations in which 14 MHz is more active during the day and 7 MHz is more active and extends to longer ranges at night. Additionally, the disruptive effects of both solar flares and geomagnetic disturbances can be readily observed. Large flares that occurred during the day had the most noticeable effects. This includes the X9.3 1153 UT 6 September flare that caused a multi-hour delay in the availability of 14 MHz and a near-complete daytime elimination of 7 MHz. Similarly, the X8.2 1535 UT 10 September flare eliminated propagation on both bands entirely for most of the day. Both of these flares had a sharp rise time and a long, multi-hour decay; the HF bands responded and recovered on similar timescales. The X1.5 1436 UT 7 September flare was also highly geoeffective, causing a deep null in 14 MHz propagation and an abrupt cutoff in 7 MHz propagation. This flare

was short lived, and 14 MHz recovered within 30 minutes. Night time flares, such as the X2.2 0857 UT 6 September flare, had minimal effect.

Figure 6 shows that the minor geomagnetic storms of 4–5 September and 12–13 September have little effect on HF propagation in the Caribbean. Following the 4–5 September storm, in which K_p remained less than 5 and SYM-H was relatively unaffected, no noticeable decrease on 14 or 7 MHz propagation was observed. Following the 12–13 September storm, in which $4 < K_p < 6$ and SYM-H dropped to -65 nT, a slight increase in spot density was observed on both HF bands. A significant negative affect on HF propagation was observed during the strong/severe storm of 7–9 September 2017. The drop in SYM-H and elevated K_p began during local evening on 7 September. Storm effects were not observed on HF immediately, as 7 MHz propagation was strong during that night and 14 MHz was not expected to be available. However, 14 MHz propagation never returned during the day on 8 September and 7 MHz propagation was poor that following night. A weak recovery on both 7 and 14 MHz took place on 9 September, but activity never returned to pre-storm levels.

Figure 7 shows that 14 and 7 MHz propagation did not return to pre-storm levels until 23 September. This is unlikely due to the affects of a single storm, but rather this compounded with the contributions of a flare and continued geomagnetic activity throughout this period. Figures 7a and 7b again show SYM-H, K_p , and GOES X-ray observations. Figure 7c shows the daily average number of 14 and 7 MHz WSPRNet and RBN spots with TX or RX endpoints in the same Caribbean region that was defined for Figure 7. Again, range is limited to $R_{gc} \leq 5000$ km. The vertical dotted line indicates the beginning of the 2100 UT 7 September storm. The blue dashed line indicates the

mean daily average for this period. Caribbean spot densities drop below the mean value on 8 September and do not exceed the mean value again until 23 September. During this time, the X8.2 10 September flare and geomagnetic activity between 12–18 September likely contribute to keeping the spot count low. To help ensure that these observations are in fact due to space weather activity and not simply lack of amateur radio operations, the global daily spot averages for this period are plotted in Figure 7d. Spots are again restricted to 14 and 7 MHz and $R_{gc} \leq 5000$ km, but no geographic filter is imposed. Additionally, daily mean values of GPS TEC in a region bounding the United States ($20^\circ \leq \phi < 55^\circ$ N and $-130^\circ \leq \theta < -160^\circ$ E) are plotted in Figure 7e. Similar to the Caribbean daily spot averages of Figure 7c, the global daily spot averages and U.S. mean GPS TEC measurements are at or below mean during the period of 8–23 September 2017.

In the Caribbean, emergency communicators suffered both the short term effects of solar flare-induced radio blackouts and the longer-term effects of geomagnetic activity-induced ionospheric storms. At times, both of these phenomena combined to make the HF communications particularly challenging. This is especially true during the 8–23 September period that began with the geomagnetic storm, when interspersed flares and geomagnetic disturbances did not allow recovery of propagation conditions for 12 to 15 days. It is likely not a single storm or flare that caused this lengthy depression in propagation, but rather a combination of multiple events.

We note a larger percentage decrease in Caribbean spots during this period compared with global observations, and therefore considered additional mechanisms to explain this drop. One possibility was increased electromagnetic noise from lightning; however, an investigation of lightning strike rates from the World Wide Lightning Location Network

(WWLLN) [Rodger *et al.*, 2006] in the Caribbean region during this time revealed that the number of strikes was low from 8–23 September 2017 compared to the pre-geomagnetic storm period of 4–8 September 2017. A more likely explanation is that in the wake of the hurricanes and other terrestrial storms, amateur radio operators were drawn away from their radios to tend to equipment damage and other aspects of disaster recovery. Still, comparison of Caribbean region observations with the global spot data gives added confidence that the general trends observed here are in fact space-weather induced.

4. Summary

Numerous solar flares and coronal mass ejection (CME) induced interplanetary shocks associated with solar active region AR12673 caused disturbances to terrestrial high frequency (HF, 3–30 MHz) radio communications from 4–14 September 2017. Simultaneously, Hurricanes Irma and Jose caused significant damage to the Caribbean Islands and parts of Florida. The coincidental timing of both the space weather activity and hurricanes was unfortunate, as HF radio was needed for emergency communications. This paper presented the response of HF amateur radio propagation as observed by the Reverse Beacon Network (RBN) and the Weak Signal Propagation Reporting Network (WSPR-Net) to space weather events of that period. Distributed data coverage from these dense sources provided a unique mix of global and regional coverage of ionospheric response and recovery that revealed several features of storm-time HF propagation dynamics. Specifically, X-class flares on 6, 7, and 10 September caused acute radio blackouts during the day in the Caribbean with recovery times of tens of minutes to hours, based on the decay time of the flare. A severe geomagnetic storm with $Kp_{max} = 8+$ and $\text{SYM-H}_{min} = -146$ nT occurring 7–10 September wiped out ionospheric communications first on 14 MHz and

then on 7 MHz starting at \sim 1200 UT 8 September. This storm, combined with effects from additional flare and geomagnetic activity, contributed to a significant suppression of effective HF propagation bands both globally and in the Caribbean for a period of 12 to 15 days.

Acknowledgments. NAF acknowledges the support of NSF Grant AGS-1552188/479505-19C75. We are especially grateful to the amateur radio community who voluntarily produced and provided the HF radio observations used in this paper, especially the operators of the Reverse Beacon Network (RBN, reversebeacon.net), the Weak Signal Propagation Reporting Network (WSPRNet, wsprnet.org), qrz.com, and hamcall.net. September 2017 amateur radio data used in this paper is available from <https://doi.org/10.5281/zenodo.1489370>; other amateur radio data is available from the source websites listed above. The K_p index was accessed through the OMNI database at the NASA Space Physics Data Facility (<https://omniweb.gsfc.nasa.gov/>). The SYM-H index was obtained from the Kyoto World Data Center for Geomagnetism (<http://wdc.kugi.kyoto-u.ac.jp/>). GOES data are provided by NOAA NCEI (<https://satdat.ngdc.noaa.gov/>). GPS based total electron content observations and the Madrigal distributed data system are provided to the community as part of the Millstone Hill Geospace Facility by MIT Haystack Observatory under NSF grant AGS-1762141 to the Massachusetts Institute of Technology. The authors wish to thank the World Wide Lightning Location Network (<http://wwlln.net>), a collaboration among over 50 universities and institutions, for providing the lightning location data used in this paper. We acknowledge the use of the Free Open Source Software projects used in this analysis: Ubuntu Linux, python [*van Rossum*, 1995], matplotlib [*Hunter*, 2007], NumPy [*Oliphant*,

2007], SciPy [Jones *et al.*, 2001], pandas [McKinney, 2010], xarray [Hoyer and Hamman, 2017], iPython [Pérez and Granger, 2007] and others [e.g. Millman and Aivazis, 2011]. NAF thanks Robert Redmon, Delores Knipp, Hyomin Kim, and Rachel Frissell for helpful discussions.

References

- ARRL (2017), Hurricane watch net to activate for Hurricane Irma.
- ARRL (2018), 2017 hurricane season after-action report.
- Benson, R. F. (1964), Electron collision frequency in the ionospheric D region, *Radio Science*, 68D(10), 1123–1126, doi:https://nvlpubs.nist.gov/nistpubs/jres/68D/jresv68Dn10p1123_A1b.pdf.
- Buonsanto, M. (1999), Ionospheric storms — a review, *Space Science Reviews*, 88(3), 563–601, doi:10.1023/A:1005107532631.
- Chakraborty, S., J. M. Ruohoniemi, J. B. H. Baker, and N. Nishitani (2018), Characterization of short-wave fadeout seen in daytime SuperDARN ground scatter observations, *Radio Science*, 53(4), 472–484, doi:10.1002/2017RS006488.
- Chamberlin, P. C., T. N. Woods, F. G. Eparvier, and A. R. Jones (2009), Next generation X-ray sensor (XRS) for the NOAA GOES-R satellite series, in *Solar Physics and Space Weather Instrumentation III*, vol. 7438, San Diego, CA, doi:10.1117/12.826807.
- Coster, A., and A. Komjathy (2008), Space weather and the Global Positioning System, *Space Weather*, 6(6), doi:10.1029/2008SW000400.
- Coster, A. J., L. Goncharenko, S.-R. Zhang, P. J. Erickson, W. Rideout, and J. Vierinen (2017), GNSS observations of ionospheric variations during the 21 August 2017 solar

eclipse, *Geophysical Research Letters*, doi:10.1002/2017GL075774, 2017GL075774.

Davies, K. (1990), *Ionospheric Radio*, Peter Peregrinus Ltd., London, England.

Davies, K., and X. M. Liu (1991), Ionospheric slab thickness in middle and low latitudes, *Radio Science*, 26(4), 997–1005, doi:10.1029/91RS00831.

Dellinger, J. H. (1937), Sudden disturbances of the ionosphere, *Proceedings of the Institute of Radio Engineers*, 25(10), 1253–1290, doi:10.1109/JRPROC.1937.228657.

Foster, J. C., P. J. Erickson, A. J. Coster, J. Goldstein, and F. J. Rich (2002), Ionospheric signatures of plasmaspheric tails, *Geophysical Research Letters*, 29(13), 1–1–1–4, doi:10.1029/2002GL015067.

Frissell, N. A., E. S. Miller, S. R. Kaepller, F. Ceglia, D. Pascoe, N. Sinanis, P. Smith, R. Williams, and A. Shovkopyas (2014), Ionospheric sounding using real-time amateur radio reporting networks, *Space Weather*, doi:<http://dx.doi.org/10.1002/2014SW001132>.

Frissell, N. A., J. D. Katz, S. W. Gunning, J. S. Vega, A. J. Gerrard, G. D. Earle, M. L. Moses, M. L. West, J. D. Huba, P. J. Erickson, E. S. Miller, R. B. Gerzoff, W. Liles, and H. W. Silver (2018), Modeling amateur radio soundings of the ionospheric response to the 2017 great american eclipse, *Geophysical Research Letters*, 45(10), 4665–4674, doi:10.1029/2018GL077324.

Fuller-Rowell, T. J., M. V. Codrescu, H. Rishbeth, R. J. Moffett, and S. Quegan (1996), On the seasonal response of the thermosphere and ionosphere to geomagnetic storms, *Journal of Geophysical Research: Space Physics*, 101(A2), 2343–2353, doi:10.1029/95JA01614.

Gibson, A. J., and P. A. Bradley (1991), A new formulation for above-the-MUF loss, in *1991 Fifth International Conference on HF Radio Systems and Techniques*, pp. 122–125.

Gonzalez, W. D., J. A. Joselyn, Y. Kamide, H. W. Kroehl, G. Rostoker, B. T. Tsurutani, and V. M. Vasyliunas (1994), What is a geomagnetic storm?, *Journal of Geophysical Research: Space Physics*, 99(A4), 5771–5792, doi:10.1029/93JA02867.

Hoyer, S., and J. Hamman (2017), xarray: N-D labeled arrays and datasets in Python, *Journal of Open Research Software*, 5(1), doi:10.5334/jors.148.

Hunter, J. D. (2007), Matplotlib: A 2d graphics environment, *Computing In Science & Engineering*, 9(3), 90–95, doi:10.1109/MCSE.2007.55.

Iyemori, T. (1990), Storm-time magnetospheric currents inferred from mid-latitude geomagnetic field variations, *Journal of Geomagnetism and Geoelectricity*, 42(11), 1249–1265, doi:10.5636/jgg.42.1249.

Jones, E., T. Oliphant, P. Peterson, et al. (2001), SciPy: Open source scientific tools for Python.

King, J., and N. Papitashvili (2006), *One Minute and Five Minute Solar Wind Data Sets at the Earth's Bow Shock Nose*, NASA Goddard Space Flight Center/Space Physics Data Facility, Greenbelt, Maryland.

Krankowski, A., I. I. Shagimuratov, and L. W. Baran (2007), Mapping of fof2 over europe based on gps-derived tec data, *Advances in Space Research*, 39(5), 651–660, doi:<https://doi.org/10.1016/j.asr.2006.09.034>.

Matsushita, S. (1959), A study of the morphology of ionospheric storms, *Journal of Geophysical Research*, 64(3), 305–321, doi:10.1029/JZ064i003p00305.

McKinney, W. (2010), Data structures for statistical computing in python, in *Proceedings of the 9th Python in Science Conference*, edited by S. van der Walt and J. Millman, pp. 51–56.

McNamara, L. F. (1979), Statistical model of the d region, *Radio Science*, 14(6), 1165–1173, doi:10.1029/RS014i006p01165.

McNamara, L. F., T. W. Bullett, E. Mishin, and Y. M. Yampolski (2008), Nighttime above-the-muf hf propagation on a midlatitude circuit, *Radio Science*, 43(2), doi:10.1029/2007RS003742.

Mendillo, M. (2006), Storms in the ionosphere: Patterns and processes for total electron content, *Reviews of Geophysics*, 44(4), doi:10.1029/2005RG000193.

Menvielle, M., and A. Berthelier (1991), The K-derived planetary indices: Description and availability, *Rev. Geophys.*, 29(3), 415–432, doi:10.1029/91RG00994.

Millman, K. J., and M. Aivazis (2011), Python for scientists and engineers, *Computing in Science & Engineering*, 13(2), 9–12, doi:10.1109/MCSE.2011.36.

Oliphant, T. E. (2007), Python for scientific computing, *Computing in Science Engineering*, 9(3), 10–20, doi:10.1109/MCSE.2007.58.

Pérez, F., and B. E. Granger (2007), IPython: a system for interactive scientific computing, *Computing in Science and Engineering*, 9(3), 21–29, doi:10.1109/MCSE.2007.53.

Poppe, B. B. (2000), New scales help public, technicians understand space weather, *Eos, Transactions American Geophysical Union*, 81(29), 322–328, doi:10.1029/00EO00247.

Prölss, G. W. (2008), *Ionospheric Storms at Mid-Latitude: A Short Review*, pp. 9–24, American Geophysical Union (AGU), doi:10.1029/181GM03.

Redmon, R. J., D. B. Seaton, R. Steenburgh, J. He, and J. V. Rodriguez (2018), September

2017's geoeffective space weather and impacts to caribbean radio communications during hurricane response, *Space Weather*, 16(9), 1190–1201, doi:10.1029/2018SW001897.

Rideout, W., and A. Coster (2006), Automated GPS processing for global total electron content data, 10(3), 219–228, doi:10.1007/s10291-006-0029-5.

Rishbeth, H. (1998), How the thermospheric circulation affects the ionospheric f2-layer, *Journal of Atmospheric and Solar-Terrestrial Physics*, 60(14), 1385 – 1402, doi:[https://doi.org/10.1016/S1364-6826\(98\)00062-5](https://doi.org/10.1016/S1364-6826(98)00062-5).

Rodger, C. J., S. Werner, J. B. Brundell, E. H. Lay, N. R. Thomson, R. H. Holzworth, and R. L. Dowden (2006), Detection efficiency of the vlf world-wide lightning location network (wwlln): initial case study, *Ann. Geophys.*, 24(12), 3197–3214, doi:10.5194/angeo-24-3197-2006.

Sckopke, N. (1966), A general relation between the energy of trapped particles and the disturbance field near the earth, *Journal of Geophysical Research*, 71(13), 3125–3130, doi:10.1029/JZ071i013p03125.

Taylor, J., and B. Walker (2010), WSPRing around the world, *QST*, 94(11), 30–32.

Thomas, E. G., J. B. H. Baker, J. M. Ruohoniemi, L. B. N. Clausen, A. J. Coster, J. C. Foster, and P. J. Erickson (2013), Direct observations of the role of convection electric field in the formation of a polar tongue of ionization from storm enhanced density, *Journal of Geophysical Research: Space Physics*, 118(3), 1180–1189, doi:10.1002/jgra.50116.

Thomas, E. G., J. B. H. Baker, J. M. Ruohoniemi, A. J. Coster, and S.-R. Zhang (2016), The geomagnetic storm time response of gps total electron content in the north american

sector, *Journal of Geophysical Research: Space Physics*, 121(2), 1744–1759, doi:10.1002/2015JA022182.

van Rossum, G. (1995), Python tutorial, *Technical Report CS-R9526*, Centrum voor Wiskunde en Informatica (CWI), Amsterdam.

Wanliss, J. A., and K. M. Showalter (2006), High-resolution global storm index: Dst versus sym-h, *Journal of Geophysical Research: Space Physics*, 111(A2), doi:10.1029/2005JA011034.

weather.com (2017), Hurricane Irma Recap, *The Weather Channel*.

Accepted Article

Approx. Wavelength [m]	Frequency [MHz]
160	1.800 - 2.000
80	3.500 - 4.000
40	7.000 - 7.300
20	14.000 - 14.350
15	21.000 - 21.450
10	28.000 - 29.700

Table 1. Selected medium and high frequency amateur radio bands. Frequency limits listed here are valid in the United States; exact frequency limits will vary based on country.

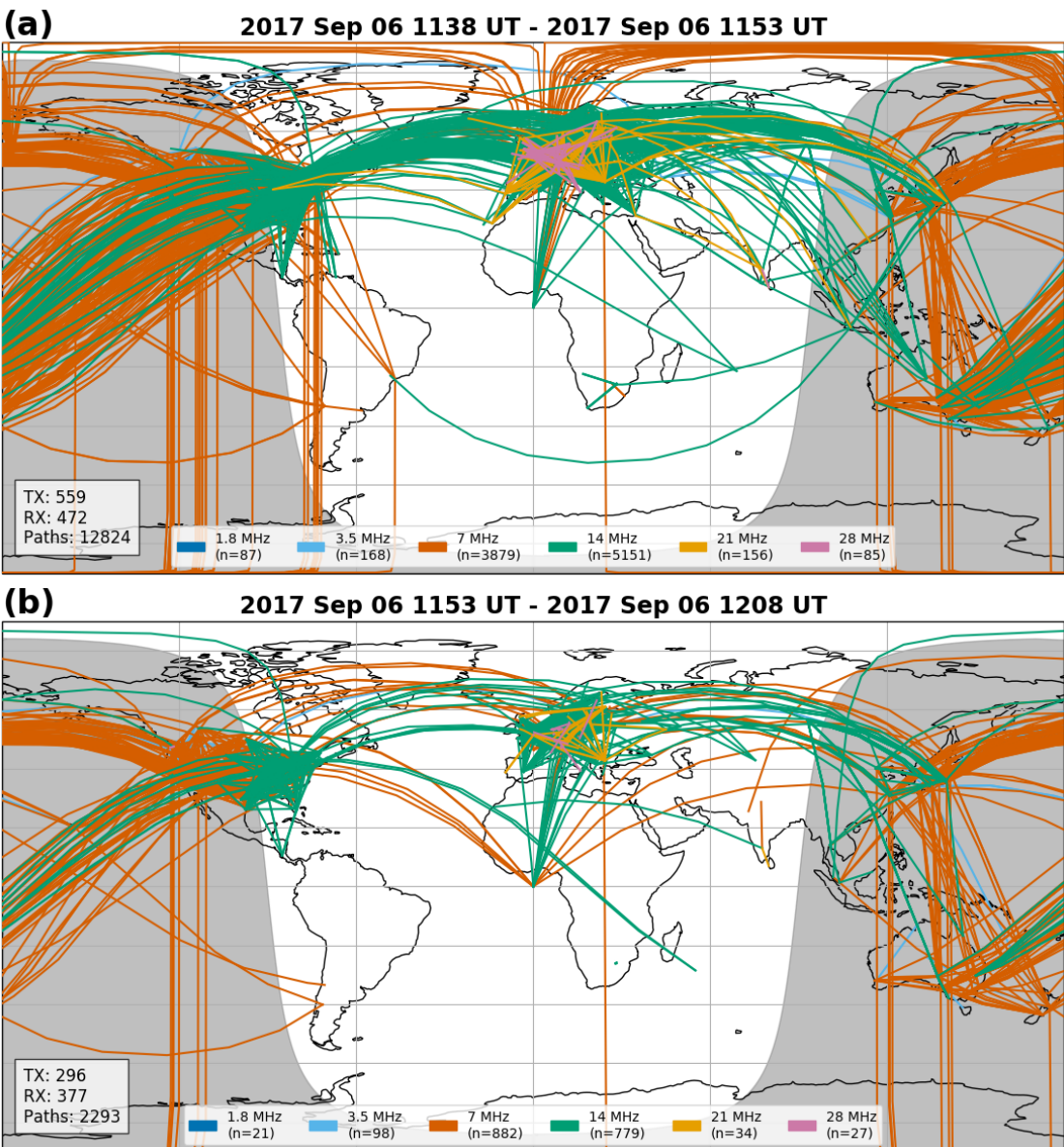


Figure 1. Amateur radio reporting network results for the (a) 15 minutes prior to and (b) 15 minutes following the X9.3 solar flare on 6 September 2017 1153 UT. The propagation paths are color-coded based on the amateur radio frequency on which the report occurred. The gray and white background shows the diurnal boundary. A reduction in reports can be seen across all frequencies with 7 MHz (dark orange), 14 MHz (bluish green), and 21 MHz (light orange) being the most affected across Europe.

06 Sep 2017
Ham Radio Networks
N Spots = 185579
RBN: 14%
WSPRNet: 86%

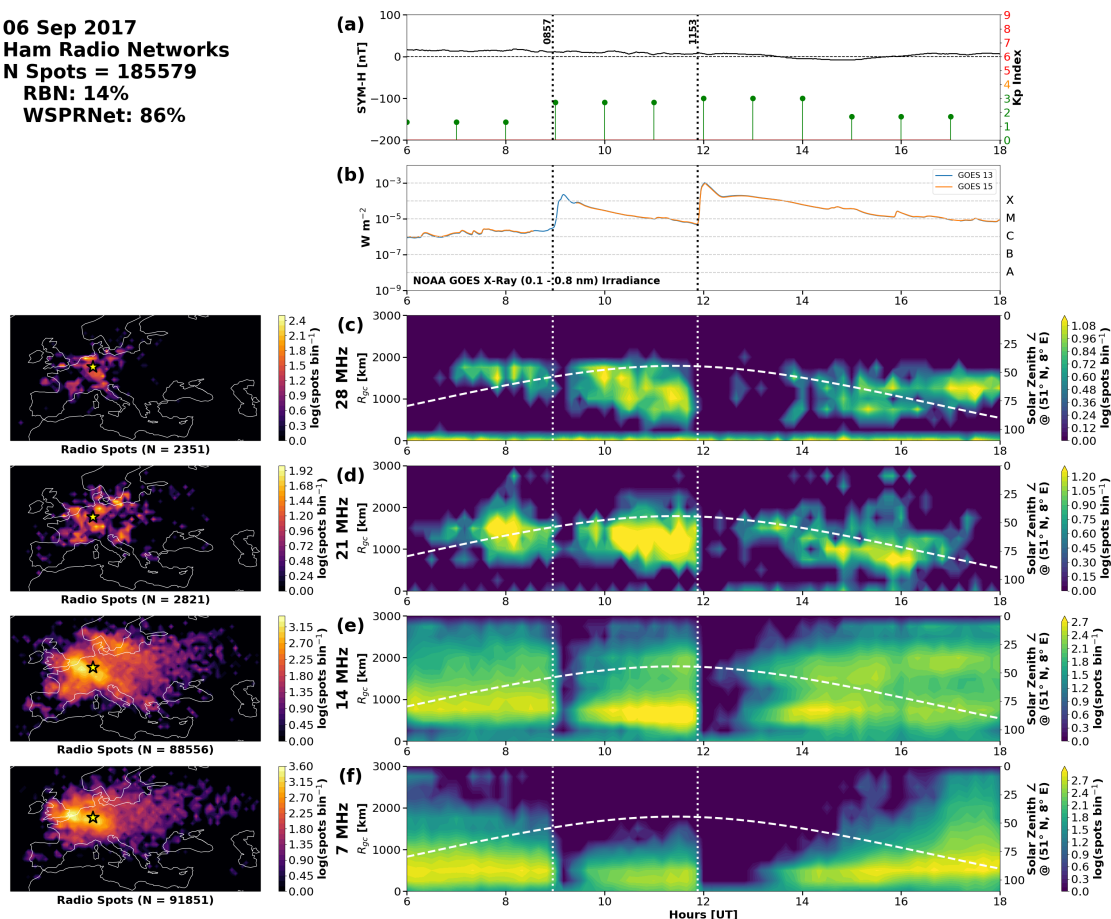


Figure 2. Space weather environment and HF radio response over Europe on 6 September 2017 0600–1800 UT. (a) SYM-H (black line) and K_p (colored stems). (b) GOES-13 (blue) and GOES-15 (orange) XRS 0.1–0.8 nm X-ray measurements. Flares are observed at 0857 UT (X2.2), 1153 UT (X9.3) and indicated with dotted vertical lines. (c–f) 2D contour histograms of RBN and WSPRNet spot data for the 28, 21, 14, and 7 MHz amateur radio bands, respectively. Bin size is 250 km x 10 min. To the left of each histogram is a map showing the log density of TX-RX midpoints of all spots used in the histogram. The white dashed lines on the histograms show the solar zenith angle computed for $(51^\circ \text{N}, 8^\circ \text{E})$, the point indicated by the yellow star on each map. Radio blackouts across the HF bands can be seen in response to the solar flares in the GOES data.

06 Sep 2017
 Ham Radio Networks
 N Spots = 50813
 RBN: 12%
 WSPRNet: 88%

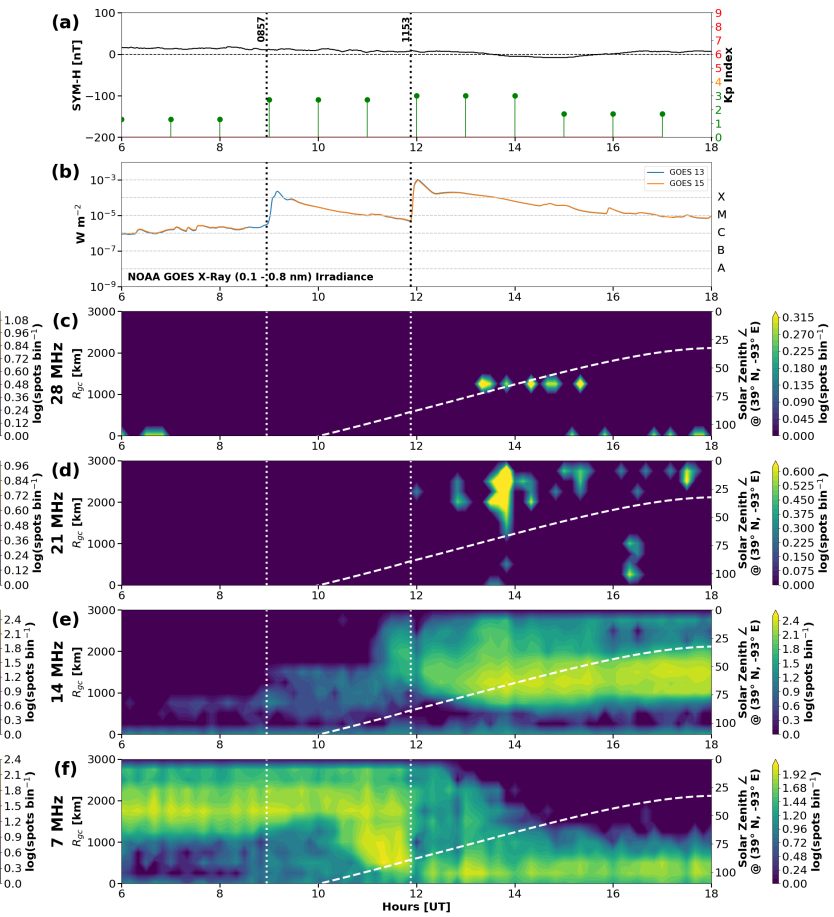
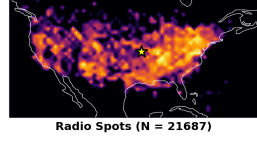
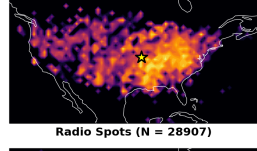
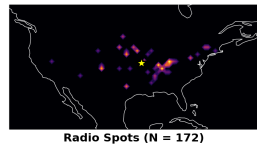
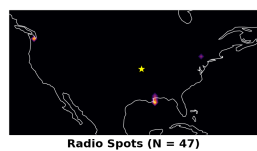


Figure 3. Space weather environment and HF radio response over the Continental United States (CONUS) on 6 September 2017 0600-1800 UT. The format is the same as for Figure 2. The X2.2 class flare at 0857 UT produces no discernible HF effect as the CONUS is still in darkness. A flare response is observed for the X9.3 class 1153 UT.

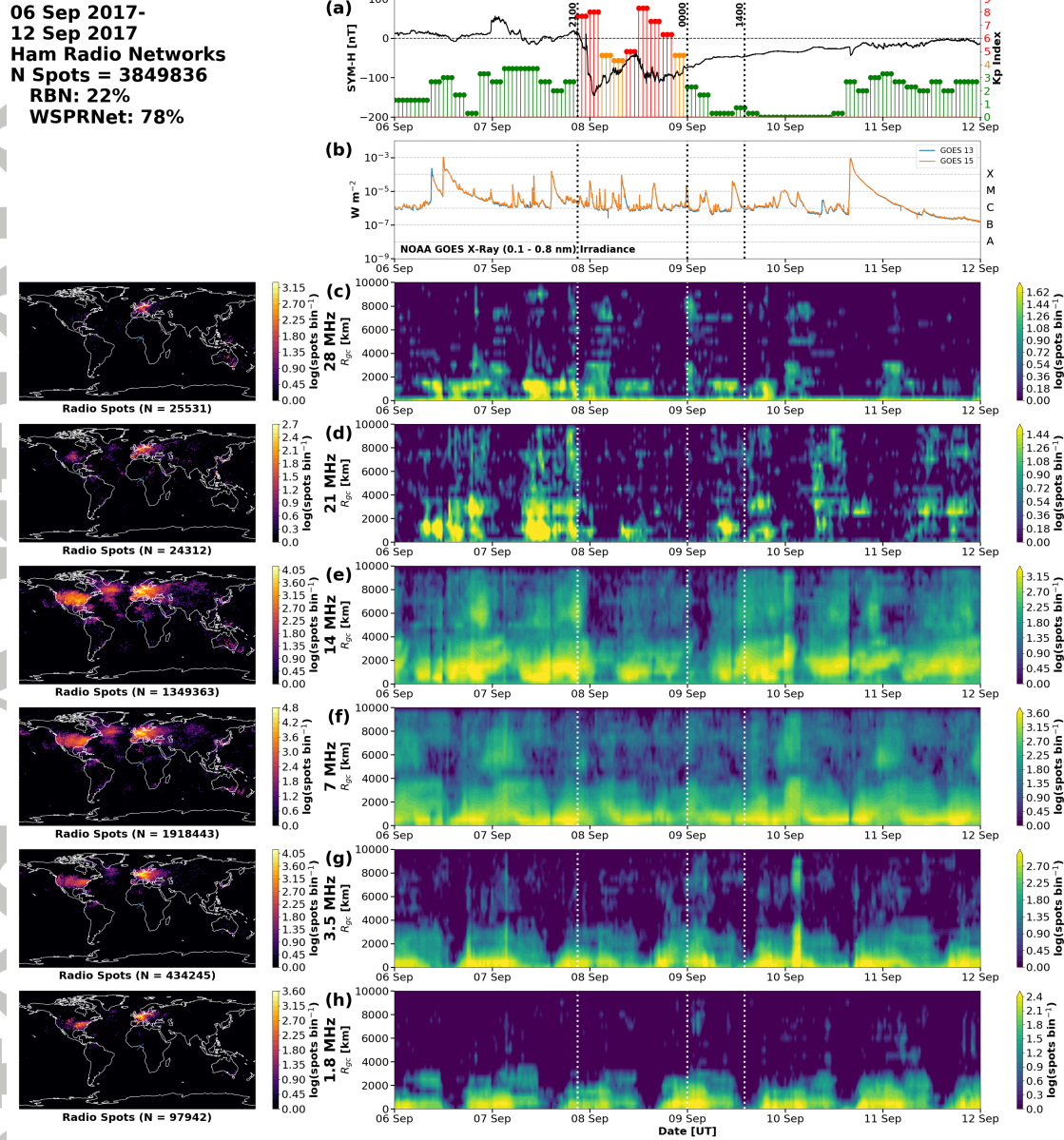


Figure 4. Space weather environment and global HF radio response from 7 September 2017–10 September 2017. (a) SYM-H (black line) and K_p (colored stems). (b) GOES-13 (blue) and GOES-15 (orange) XRS 0.1–0.8 nm X-ray measurements. (c–h) 2D contour histograms of RBN and WSPRNet spot data on a log scale for the 28, 21, 14, 7, 3.5, and 1.8 MHz amateur radio bands, respectively. To the left of each histogram is a map showing the TX-RX midpoints (blue dots) of all spots used in the histogram. Vertical dotted lines indicate (2100 UT 7 September) start of disturbed K_p , (0000 UT 9 September) end of disturbed K_p , and (1400 UT 9 September) apparent HF recovery.

06 Sep 2017-
12 Sep 2017
Ham Radio Networks
N Spots = 3849836
RBN: 22%
WSPRNet: 78%

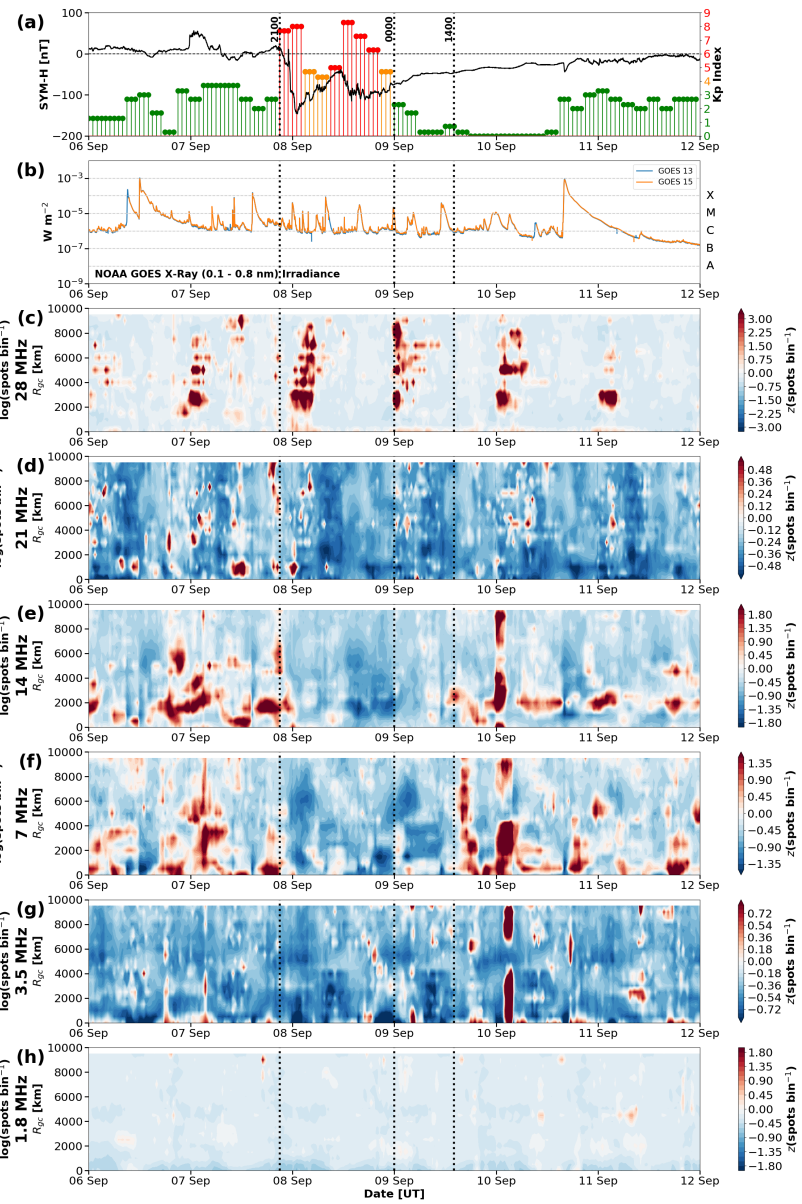
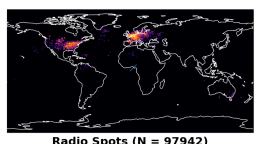
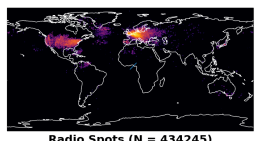
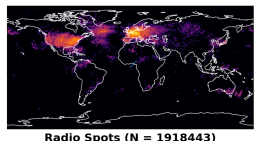
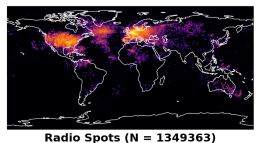
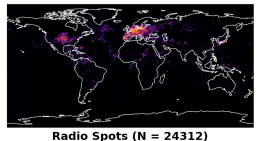
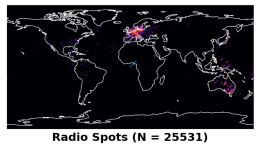


Figure 5. z -score of Figure 4. Format is the same as Figure 4. Quiet time mean and standard deviation day was computed from 2016 and 2017 WSPRNet and RBN data. See Section 3.2 for details.

04 Sep 2017-
14 Sep 2017
Ham Radio Networks
N Spots = 71856
RBN: 18%
WSPRNet: 82%

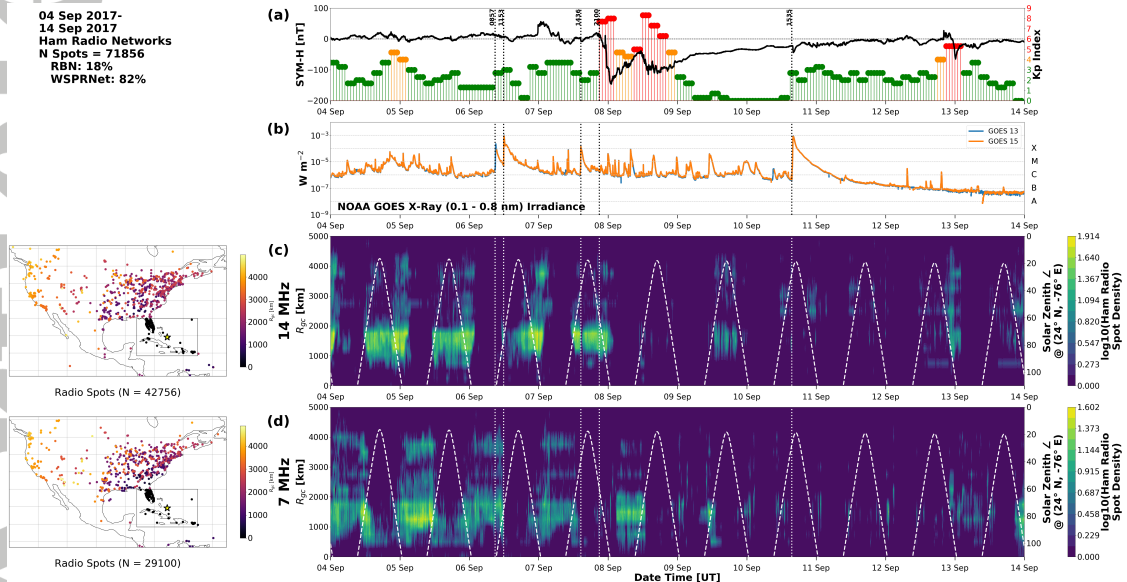


Figure 6. Space weather environment and HF radio response for the Caribbean region from 4–14 September 2017. (a) SYM-H (black line) and K_p (colored stems). (b) GOES-13 (blue) and GOES-15 (orange) 0.1–0.8 nm X-ray measurements. (c–d) 2D contour histograms of RBN and WSPRNet spot data on a log scale for the 14 and 7 MHz amateur radio bands, respectively. To the left of each histogram is a map showing the endpoints of all spots used in the histogram. Black dots in each map represent endpoints contained within the Caribbean region (black box). Corresponding endpoints outside of the Caribbean region are identified by dots color-coded with the great circle path length R_{gc} of each link. The white dashed lines on the histograms show the solar zenith angle computed for $(24^\circ \text{ N}, 76^\circ \text{ E})$, the point indicated by the yellow star in the center of the Caribbean box. The 28, 21, 3.5, and 1.8 MHz are not shown as they each have < 1000 spots for the entire interval.

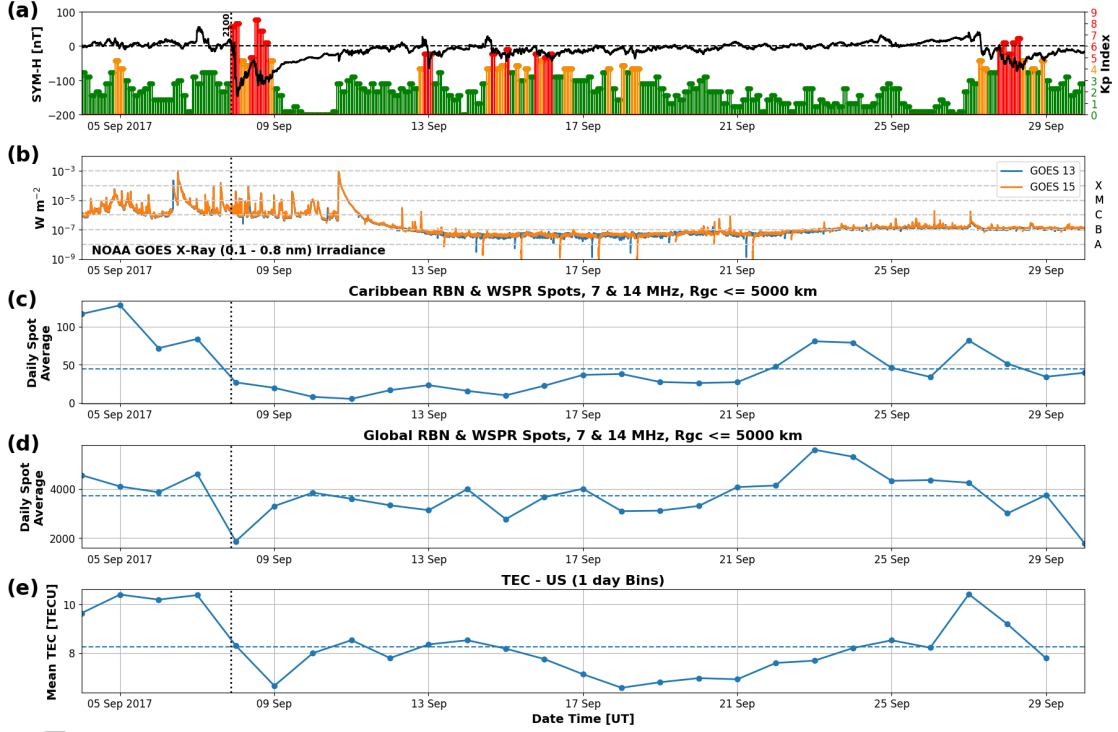


Figure 7. Space weather environment and HF radio response for the Caribbean region from 4–30 September 2017. (a) SYM-H (black line) and K_p (colored stems). (b) GOES-13 (blue) and GOES-15 (orange) 0.1–0.8 nm X-ray measurements. (c) Daily average of RBN and WSPRNet ham radio spots with TX or RX endpoints in the Caribbean region on 7 and 14 MHz with $R_{gc} \leq 5000$ km. (d) Daily average of global 7 and 14 MHz RBN and WSPRNet spots with $R_{gc} \leq 5000$ km. (e) Daily average GPS TEC for a region bounding the United States ($20^\circ \leq \phi < 55^\circ$ N and $-130^\circ \leq \theta < -160^\circ$ E). The dashed blue lines in (c), (d), and (e) shows the mean of each panel for the plotted interval.